

Revisiting Carbon Flux Through the Ocean's Twilight Zone

Ken O. Buesseler,^{1*} Carl H. Lamborg,¹ Philip W. Boyd,² Phoebe J. Lam,¹ Thomas W. Trull,³ Robert R. Bidigare,⁴ James K. B. Bishop,^{5,6} Karen L. Casciotti,¹ Frank Dehairs,⁷ Marc Elskens,⁷ Makio Honda,⁸ David M. Karl,⁴ David A. Siegel,⁹ Mary W. Silver,¹⁰ Deborah K. Steinberg,¹¹ Jim Valdes,¹² Benjamin Van Mooy,¹ Stephanie Wilson¹¹

The oceanic biological pump drives sequestration of carbon dioxide in the deep sea via sinking particles. Rapid biological consumption and remineralization of carbon in the “twilight zone” (depths between the euphotic zone and 1000 meters) reduce the efficiency of sequestration. By using neutrally buoyant sediment traps to sample this chronically understudied realm, we measured a transfer efficiency of sinking particulate organic carbon between 150 and 500 meters of 20 and 50% at two contrasting sites. This large variability in transfer efficiency is poorly represented in biogeochemical models. If applied globally, this is equivalent to a difference in carbon sequestration of more than 3 petagrams of carbon per year.

The transfer efficiency of the biological pump (I) depends upon how much sinking particulate organic carbon (POC) is remineralized and consumed by resident biota within the ocean's twilight zone. This downward POC flux in the ocean comprises a complex mixture of living and dead cells, excretory products, detrital matter, and amorphous aggregates (2). Remineralization of POC and associated bioelements sets the concentration of deep ocean nutrients and via subsequent upwelling is a feedback on the strength of primary productivity. Since the 1980s there have been various attempts to parameterize this flux attenuation (3), the most common being $F = F_{100}(z/100)^{-b}$, where z is the trap depth, F_{100} is the POC flux at 100 m, and b is a unitless parameter determining

the degree of flux attenuation with depth. A single empirical fit using six North Pacific sites yielded the Martin curve, with $F_{100} = 4.2 \text{ mM C m}^{-2} \text{ day}^{-1}$ and $b = 0.86$ (4), which is still widely used in models to describe particle flux attenuation across regions and also globally (5–7).

In the past 10 to 20 years, concerns have grown over the validity of the Martin curve due in part to the possibility of collection biases in upper ocean sediment traps, which are open cylinders or cones, tethered to surface floatation, used to directly sample sinking particles (8). Moreover, flux predictions from global circulation and data assimilation models (9, 10) and measurements of flux variability in the deep ocean (11) have questioned the global applicability of this flux curve. Alternatives have since been proposed (11, 12), but their value is unclear because they have their basis largely in models and/or traps in the deep ocean, where flux collection biases are reduced but particle flux attenuation is much weaker (13).

VERTIGO (Vertical Transport in the Global Ocean). The VERTIGO project overcame many of the issues of trap collection biases in mesopelagic waters by using neutrally buoyant sediment traps (NBSTs) (14). These new-generation particle interceptors address the hydrodynamic concern of particle capture in a fluid moving several orders of magnitude faster laterally (km per day) than mean particle sinking rates (10 to 100 m day⁻¹) (2). NBSTs are free vehicles that sink to a predetermined depth, directly intercepting sinking particles in collection tubes for a preset period (days), after which the tubes close and the NBSTs surface (15) (figs. S1 and S2). We deployed NBSTs twice for 3 to 5 days using two to three instruments per depth (150 m for 3 days, 300 m for 4 days, and 500 m for 5 days). Such replication of flux measurements is rarely done. Another unique facet of

VERTIGO was the 21-day occupation of each study site, which enabled us, with replicate deployments, to relate changes in flux at 500 m to processes in the surface water occurring several days prior [the majority of particles sink >100 m day⁻¹ (16) and thus would reach 500 m within ~5 days].

VERTIGO studied two contrasting environments. ALOHA is within an oligotrophic subtropical gyre and is the site of the Hawaii Ocean time series (HOT) (17). At ALOHA, consistently low macronutrients within a warm surface ocean result in an ecosystem dominated by picophytoplankton and low seasonality, with relatively low and constant rates of primary production and POC flux at the base of the euphotic zone. K2 is situated in the Northwest Pacific subarctic gyre and is the site of a moored time-series program (18). K2 is characterized by colder waters and high nutrient conditions, resulting in more seasonality in algal stocks, production, and export (18). Another important contrast is that the biomineral content of sinking particles at ALOHA was dominated by particulate inorganic carbon (PIC, i.e., carbonate contents of 30% at 500 m and 60% at 4000 m, Table 1), whereas fluxes at K2 during summer were dominated by biogenic silica (bSi, i.e., opal) because of surface diatom productivity (80% at 500 and 4000 m).

K2 had higher POC fluxes than ALOHA at all depths (Fig. 1A). Fluxes at ALOHA were similar during both trap deployments, whereas at K2 POC flux decreased threefold between the two deployments, indicating substantial temporal phasing of export at this site. The normalized flux profiles display lower POC flux attenuation at K2 than at ALOHA (Fig. 1B). POC flux profiles from both K2 deployments collapse onto each other upon normalization to flux at 150 m (Fig. 1B), despite their difference in POC flux. This suggests that POC flux attenuation is not determined by the magnitude of flux but rather by the nature of the exported POC and the processes within the mesopelagic that are site specific. The degree of flux attenuation can be expressed as mesopelagic transfer efficiency (T_{eff}) or the ratio of POC flux at 500 to 150 m. At ALOHA, T_{eff} is only 20%, whereas for K2 T_{eff} equals 46 to 55% (Table 1).

This pattern of more rapid POC flux attenuation at ALOHA versus K2 holds for all associated bioelements and follows an internally consistent pattern (Fig. 2). At each site, attenuation follows the same relative order, with chlorophyll *a* > POC > particle mass > bSi > PIC, and tracks the lability of these elements, with phytodetrital flux decreasing fastest and much smaller losses of biominerals such as bSi and PIC as they sink. This implies that, for each component within the sinking particles, a larger proportion would sink to greater depth if associated with biomineral phases. All particle-associated elements reach greater depth at K2, which would enhance C sequestration at K2

¹Department of Marine Chemistry and Geochemistry, Woods Hole Oceanographic Institution, Woods Hole, MA 02543, USA. ²National Institute of Water and Atmospheric Research Centre for Physical and Chemical Oceanography, Department of Chemistry, University of Otago, Dunedin, New Zealand. ³Antarctic Climate and Ecosystems Cooperative Research Centre, University of Tasmania and Commonwealth Scientific and Industrial Research Organisation, Marine and Atmospheric Research, Hobart, 7001, Australia. ⁴Department of Oceanography, University of Hawaii, Honolulu, HI 96822, USA. ⁵Earth Sciences Division, Lawrence Berkeley National Laboratory, Berkeley, CA 94720, USA. ⁶Department of Earth and Planetary Science, University of California, Berkeley, CA 94720, USA. ⁷Analytical and Environmental Chemistry, Free University of Brussels, B-1050 Brussels, Belgium. ⁸Japan Agency for Marine-Earth Science and Technology (JAMSTEC), Mutsu Institute for Oceanography, Yokosuka, Kanagawa 237-0061, Japan. ⁹Institute for Computational Earth System Science, University of California, Santa Barbara, CA 93106, USA. ¹⁰Ocean Sciences Department, University of California, Santa Cruz, CA 95064, USA. ¹¹Virginia Institute of Marine Science, College of William and Mary, Gloucester Point, VA 23062, USA. ¹²Department of Physical Oceanography, Woods Hole Oceanographic Institution, Woods Hole, MA 02543, USA.

*To whom correspondence should be addressed. E-mail: kbuesseler@whoi.edu

relative to ALOHA and consequently result in greater remineralization length scales at K2 for nutrients such as silicate.

The differences in particle flux attenuation between K2 and ALOHA must be related to the properties that characterize each site. These include pelagic food web structure, the proportion of fecal pellets versus phytoplankton aggregates, the fraction of export associated with ballast minerals and their sinking rates, water temperature, and C demand of the mesopelagic bacteria and zooplankton communities, or combinations thereof. Also, higher zooplankton abundances at K2 will have an impact on C transfer to depth via surface feeding and daily migration to mesopelagic depths.

Our observations demonstrate that the diatom-dominated ecosystem at K2 is associated with more efficient transport of POC through the twilight zone than the ecosystem at ALOHA. In addition to the high T_{eff} in the mesopelagic, the high efficiency of this “silica pump” in the Northwest Pacific for POC transport to the deep ocean has been noted previously (19). Thus, our mesopelagic data contrast with predictions of the POC-carrying efficiency of different ballasting agents developed by using bathypelagic trap data, which suggested preferential deep ocean POC flux in association with PIC and not bSi (11, 20).

The structure of the food web can also change temporally at any given site. Forty days after peak diatom production at K2 (18), we observed a continued decrease in primary production and a decrease in the fraction of C fixation attributable to $>20\ \mu\text{m}$ phytoplankton during deployment 2 (Table 1). A decrease in the export ratio from 21 to 11% [e ratio is trap-derived flux at base of euphotic zone divided by primary productivity (PP)] fits with lower export predicted with a shift to smaller cells (21, 22). The constant T_{eff} at K2 in a changing flux environment suggests that flux attenuation processes below the euphotic zone respond proportionally and rapidly to the flux.

During both K2 deployments, most of the identifiable material intercepted by traps was fecal matter from larger zooplankton, in particular copepod species. In the water column above the traps at K2, both zooplankton size and the median size of fecal pellets were significantly larger (42% of zooplankton biomass from 0 to 150 m was $>2\ \text{mm}$; $0.17\ \mu\text{g C}$ per pellet at 150 m; fig. S3) than at ALOHA (18% of biomass was $>2\ \text{mm}$; $0.036\ \mu\text{g C}$ per pellet). Larger pellets tend to have higher gravitational sinking rates (3). Sinking rates would be further increased by the higher percentage of more dense biomineral phases within the sinking particles at K2 (80% opal and carbonate by mass at K2 versus 21% at ALOHA in 150-m trap; Table 1), although slower settling rates in colder, more viscous waters are a potential factor that would offset some of these density-driven changes in sinking rate. Therefore, a simple explanation that may account for much of the twofold higher T_{eff} at K2

compared with that at ALOHA is a faster sinking rate due to differences in ballasting and zooplankton pellet size. The impact of colder temperatures on the rate of heterotrophic metabolism may also contribute to this higher T_{eff} at K2 because of slower biological degradation of sinking particles.

The extent of flux attenuation at the two VERTIGO sites is not captured by the Martin curve. After normalizing the observed flux to 150 m, average b values for POC at ALOHA ($b = 1.33 \pm 0.15$; fitted value \pm 1 SE) are higher than predicted (4), indicating greater flux attenuation, and lower at K2 ($b = 0.51 \pm 0.05$), indicating more efficient C transfer to depth (Fig. 1B). Indeed, the contrast in POC flux attenuation between ALOHA and K2 exceeds the range seen across the six sites used to derive the Martin curve (b ranged from 0.64 to 0.97) (4). Applying

the Martin curve at ALOHA would result in a POC flux at 500 m that is double (i.e., $36\ \text{mg C m}^{-2}\ \text{day}^{-1}$) our observations. At K2, POC fluxes would be 50% too small. The same over- and underpredictions would hold for other elements as well (Fig. 2) and thus would impact relative ratios of nutrients associated with remineralization of sinking particles.

Recent modeling studies based on extensive WOCE nutrient and alkalinity data (10) suggest that geochemical distributions in the deep ocean are highly sensitive to the choice of POC flux parameterization. By using global circulation models and simulated export production, Howard *et al.* (10) found differences of $>60\ \mu\text{mol}$ dissolved inorganic carbon (DIC) kg^{-1} in the deep ocean between models and observations by using a Martin-like flux parameterization and increases of $30\ \mu\text{mol DIC kg}^{-1}$ by increasing the

Table 1. VERTIGO site characteristics (14). Temp. is temperature, S is salinity, and dep. is trap deployment. ALOHA O_2 taken from HOT bottle data average for June and July 2004. POM is particulate organic matter and is calculated to be equal to 2.2 times mass of POC (20). Opal is calculated to be equal to mg of bSi times 2.4 (26). CaCO_3 is equal to 8.33 times PIC. Deep particle properties for ALOHA are from annual averages from a 4280-m trap [15.5°N , 151.5°E ; Honjo *et al.* (27)], whereas K2 data are from 4810-m K2 trap samples corresponding to a VERTIGO cruise in 2005. Primary production from VERTIGO cruises are based on shipboard deck incubations using ^{14}C and ^{13}C methods and integrated to the 0.1% light level. For ALOHA, these are within 95% confidence intervals for HOT PP data for upper 100 m but >2 times lower than in situ PP on HOT cruises before and after VERTIGO. K2 PP are higher (D1) and similar to PP estimated by Honda *et al.* (18) for the same time period. Size-fractionated PP calculated as the percent of total PP attributable to $>20\text{-}\mu\text{m}$ cells. Euphotic zone e ratio uses POC flux at 0.1% light level extrapolated using POC flux curve fits (Fig. 1) to mesopelagic data. Measured 150-m flux/PP ratios are 10 and 8% for ALOHA D1 and D2, and 12 and 6% for K2 D1 and D2, respectively. Mesopelagic transfer efficiency defined as 500-m/150-m POC flux.

	ALOHA			K2		
Dates on site	22 June to 9 July 2004			22 July to 18 August 2005		
Deployment start dates	23 June and 2 July 2004			30 July and 10 August 2005		
Mixed layer depth	49 m			26 m		
Depth of 0.1% light	~125 m			~50 m		
	<i>Physical properties</i>					
	Temp. ($^\circ\text{C}$)	S	O_2 (μM)	Temp. ($^\circ\text{C}$)	S	O_2 (μM)
Mixed layer	26.10	34.63	210	9.61	32.91	285
150 m	21.93	35.26	204	2.17	33.46	198
300 m	13.55	34.33	210	3.37	33.97	29
500 m	7.62	34.04	115	3.17	34.18	21
1000 m	3.94	34.45	45	2.57	34.43	21
	<i>Particle properties (average by weight)</i>					
	% POM	% CaCO_3	% Opal	% POM	% CaCO_3	% Opal
150 m	63.9	13.3	7.7	17.2	3.6	76.8
300 m	51.6	27.1	11.4	13.2	3.2	81.8
500 m	54.9	31.9	16.3	14.1	3.4	80.4
4000 m	13.3	59.9	26.9	7.6	8.5	77.0
	<i>POC fluxes ($\text{mg m}^{-2}\ \text{day}^{-1}$)</i>					
	First dep.	Second dep.		First dep.	Second dep.	
Integrated PP	180	220		530	365	
150-m POC flux	18	18		62	23	
300-m POC flux	7.2	6.0		47	17	
500-m POC flux	3.6	3.6		29	13	
	<i>Production, export, and flux ratios</i>					
	First dep.	Second dep.		First dep.	Second dep.	
% PP $>20\ \mu\text{m}$	12%	11%		30%	19%	
e ratio = flux at 0.1% light/PP	13%	11%		21%	11%	
$T_{\text{eff}} = 500\text{-m}/150\text{-m flux}$	20%	21%		46%	55%	

T_{eff} by a factor of 2.5. VERTIGO data confirm the existence of regional differences in POC T_{eff} of twofold or more. Our sites represent low-latitude oligotrophic and high-latitude mesotrophic regions and thus are unlikely to be biogeochemical end members for the global ocean or even seasonal extremes at these two sites.

Implications and conclusions. Our high and low T_{eff} s, if applied to the global shallow export production estimate of Laws *et al.* of 11 Pg C year⁻¹ (23), would result in a POC flux at 500 m ranging from 2.3 to 5.5 Pg C year⁻¹ or a difference in ocean C sequestration below 500 m

of more than 3 Pg C year⁻¹. For comparison, global anthropogenic emissions of C are 6 to 7 Pg C year⁻¹. Certainly the entire ocean is not characterized by either single T_{eff} ; however, this calculation shows that, in addition to climate-induced changes to primary production, floristics, and shallow export, changes to mesopelagic communities and T_{eff} would have a large impact on the magnitude of ocean C sequestration and hence be a substantial feedback on climate. The predicted increase in ocean stratification and the decrease in nutrient supply because of climate change are thought to favor small phytoplankton at the expense of diatoms

(24). Also, a decrease in ocean pH with increased CO₂ would tend to decrease the fraction of ocean production attributed to calcium carbonate producers (25). Both of these effects would result in not only less-efficient shallow export production but also likely lower mesopelagic T_{eff} and hence reduce ocean C sequestration, which would greatly amplify this positive feedback on climate change.

These data help connect surface-water particle sources to mesopelagic fluxes. Both the fraction of production leaving the surface and the proportion of export reaching the deep ocean are highly variable and of similar importance to the sequestration of C in the deep ocean. Although process studies at contrasting sites using NBSTs can help unravel differences in particle flux attenuation and its controls, mesopelagic time-series observations are necessary to catch episodic events and the full range of flux variability. This variability in the attenuation of sinking particle flux is not yet considered in ocean models and is poorly constrained by existing data from the twilight zone.

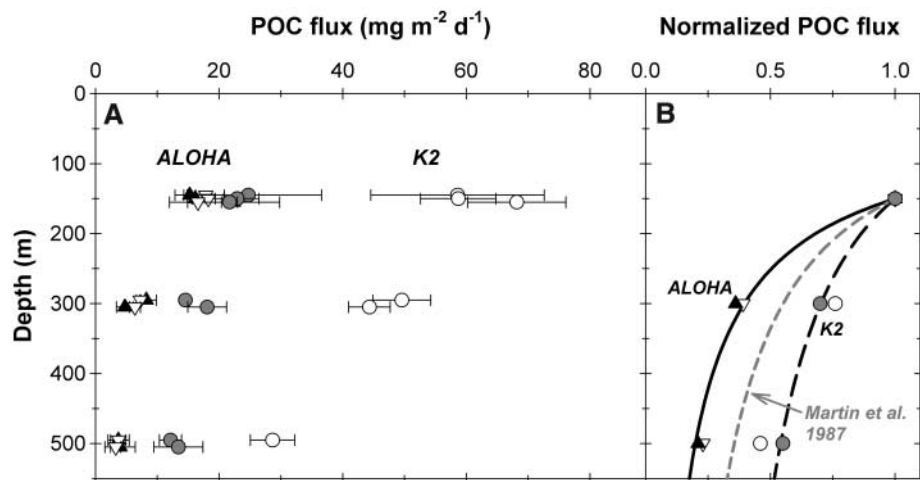
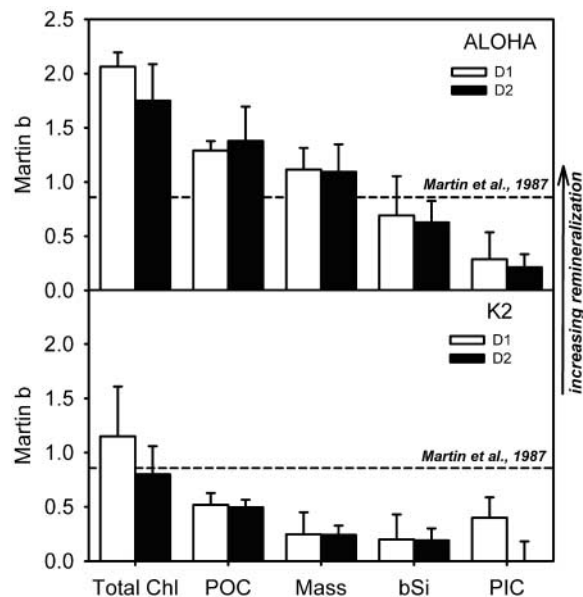


Fig. 1. POC flux versus depth at ALOHA (22° 45' N, 158° W) and K2 (47° N 160° E). (A) POC flux at ALOHA (triangles) and K2 (circles) with open and solid symbols for deployments 1 and 2, respectively (deployment start dates in Table 1). (B) Same data normalized to 150 m POC flux and compared with Martin *et al.* (4) (dashed line). For each depth, up to three independent NBSTs were deployed from the same launch site, and the POC fluxes are shown (A) for each NBST, with a slight vertical offset, as the mean and standard deviation of replicate POC measurements (n from 2 to 4). Fits to normalized data (B) used a power function of the form $F/F_{150} = (z/150)^{-b}$, where z is the depth of the trap, F_{150} is the POC flux at the 150-m reference depth, and b describes the rate of flux attenuation.

Fig. 2. Relative rates of flux attenuation as parameterized by power law fit of Martin *et al.* (4) for chlorophyll *a*, POC, mass, bSi, and PIC. These are calculated for deployment 1 (open) and 2 (solid) for ALOHA (top) and K2 (bottom), with an error bar derived from the curve fit to multiple NBST flux data at three depths. Also shown for comparison as a horizontal dashed line is the b value for the Martin curve of 0.86, with larger values of b indicating faster flux attenuation, i.e., increasing remineralization.



References and Notes

1. T. Volk, M. I. Hoffert, *Geophys. Monogr. Am. Geophys. Union* 32 (American Geophysical Union, Washington, DC, 1985).
2. S. W. Fowler, G. A. Knauer, *Prog. Oceanogr.* **16**, 147 (1986).
3. J. Bishop, in *Productivity of the Ocean: Present and Past*, W. H. Berger, V. S. Smetacek, G. Wefer, Eds. (Wiley, New York, 1989), pp. 117–138.
4. J. H. Martin, G. A. Knauer, D. M. Karl, W. W. Broenkow, *Deep-Sea Res. A* **34**, 267 (1987).
5. R. W. Najjar, J. L. Sarmiento, J. R. Toggweiler, *Global Biogeochem. Cycles* **6**, 45 (1992).
6. Y. Yamanaka, E. Tajika, *Global Biogeochem. Cycles* **10**, 361 (1996).
7. T. Ito, M. J. Follows, *J. Mar. Res.* **63**, 813 (2005).
8. K. O. Buesseler, *Nature* **353**, 420 (1991).
9. R. Schlitzer, *Deep-Sea Res. II* **49**, 1623 (2002).
10. M. T. Howard, A. M. E. Winguth, C. Klaas, E. Maier-Reimer, *Global Biogeochem. Cycles* **20**, GB3011 (2006).
11. R. Francois, S. Honjo, R. Krishfield, S. Manganini, *Global Biogeochem. Cycles* **16**, 1087 (2002).
12. R. A. Armstrong, C. Lee, J. I. Hedges, S. Honjo, S. G. Wakeham, *Deep-Sea Res. II* **49**, 219 (2002).
13. P. W. Boyd, T. W. Trull, *Prog. Oceanogr.* 10.1016/j.pcean.2006.10.1007 (2006).
14. Materials and methods are available on Science Online.
15. K. O. Buesseler *et al.*, *Deep-Sea Res. I* **47**, 277 (2000).
16. T. Trull *et al.*, in *ASLO-TOS-AGU Ocean Sciences Meeting Abstracts*, abstr. 0523H-05 (2006).
17. D. M. Karl *et al.*, *Deep-Sea Res. II* **43**, 539 (1996).
18. M. C. Honda, H. Kawakama, K. Sasaoka, S. Watanabe, T. Dickey, *Geophys. Res. Lett.* **33**, L16603 (2006).
19. M. C. Honda, *J. Oceanogr.* **59**, 671 (2003).
20. C. Klaas, D. E. Archer, *Global Biogeochem. Cycles* **16**, 1116 (2002).
21. A. F. Michaels, M. W. Silver, *Deep-Sea Res.* **35**, 473 (1988).
22. R. Peinert, B. von Bodungen, V. S. Smetacek, in *Productivity of the Ocean: Present and Past*, W. H. Berger, V. S. Smetacek, G. Wefer, Eds. (Wiley, New York, 1989), pp. 35–48.
23. E. A. Laws, P. G. Falkowski, W. O. Smith Jr., H. Ducklow, J. J. McCarthy, *Global Biogeochem. Cycles* **14**, 1231 (2000).

24. L. Bopp, O. Aumont, P. Cadule, S. Alvain, M. Gehlen, *Geophys. Res. Lett.* **32**, 10.1029/2005GL023653 (2005).
 25. R. A. Feely *et al.*, *Science* **305**, 362 (2004).
 26. R. A. Mortlock, P. N. Froelich, *Deep-Sea Res. A* **36**, 1415 (1989).
 27. S. Honjo, S. J. Manganini, J. J. Cole, *Deep-Sea Res. A* **29**, 609 (1982).
 28. VERTIGO would not have been possible without the field support obtained from the captain, crew, and shore-based support for the R/V *Kilo Moana* (2004) and R/V *Roger Revelle* (2005). Funding was obtained primarily through the NSF, Ocean Sciences Programs

in Chemical and Biological Oceanography, with additional support from the U.S. Department of Energy, Office of Science, Biological and Environmental Research Program, and other national programs, including the Australian Cooperative Research Centre program and Australian Antarctic Division. In addition, there are a number of individuals whose efforts at sea or in the laboratory made this VERTIGO program possible, including J. Andrews, C. Bertrand, R. Bidigare III, S. Bray, K. Casciotti, M. Charette, S. Coale, J. Cope, E. Fields, M. Gall, G. Jiao, T. Kobari, S. Saitoh, M. Sarin, S. Manganini, C. Moy, S. Okamoto, S. Pike,

L. Robertson, D. Ruddick, and Y. Zhang. We also thank the reviewers for their comments. More information can be found at <http://cafeatorium.whoi.edu>.

Supporting Online Material

www.sciencemag.org/cgi/content/full/316/5824/567/DC1
 Materials and Methods
 SOM Text
 Figs. S1 to S3
 References

27 November 2006; accepted 8 March 2007
 10.1126/science.1137959

A Selective Activity-Dependent Requirement for Dynamin 1 in Synaptic Vesicle Endocytosis

Shawn M. Ferguson,^{1,2,3} Gabor Brasnjo,^{5*} Mitsuko Hayashi,^{1,2,3*} Markus Wölfel,³ Chiara Collesi,^{1,2,3,7} Silvia Giovedi,^{1,2,3} Andrea Raimondi,^{1,2,3} Liang-Wei Gong,^{1,2,3} Pablo Ariel,^{5,6} Summer Paradise,^{1,2,3} Eileen O'Toole,⁸ Richard Flavell,^{1,4} Ottavio Cremona,⁷ Gero Miesenböck,³ Timothy A. Ryan,⁵ Pietro De Camilli^{1,2,3,†}

Dynamin 1 is a neuron-specific guanosine triphosphatase thought to be critically required for the fission reaction of synaptic vesicle endocytosis. Unexpectedly, mice lacking dynamin 1 were able to form functional synapses, even though their postnatal viability was limited. However, during spontaneous network activity, branched, tubular plasma membrane invaginations accumulated, capped by clathrin-coated pits, in synapses of dynamin 1–knockout mice. Synaptic vesicle endocytosis was severely impaired during strong exogenous stimulation but resumed efficiently when the stimulus was terminated. Thus, dynamin 1–independent mechanisms can support limited synaptic vesicle endocytosis, but dynamin 1 is needed during high levels of neuronal activity.

Synaptic transmission is dependent on the continuous reformation of synaptic vesicles via local membrane recycling (1, 2). Although the precise mechanisms of synaptic vesicle reformation remain a matter of debate (3–7), there is strong evidence for a key role of the guanosine triphosphatase (GTPase) dynamin in this process (8–12), as well as in a variety of endocytic reactions in all cell types (9, 13–16). Dynamin is thought to oligomerize at the neck of endocytic pits and to mediate neck constriction

and fission (8, 9, 11). However, previous studies have addressed the action of dynamin at synapses through dominant-negative interference or pharmacological inhibition strategies, which may also elicit dominant-negative effects from the inactivated protein. Thus, we investigated the importance of dynamin in membrane traffic at synapses in dynamin 1–null mutants.

Mammals express three dynamins with different expression patterns (fig. S1) (17). Dynamin 1 is expressed exclusively in the brain, whereas dynamin 2 is ubiquitously expressed, and dynamin 3 is expressed selectively in brain and testis (fig. S1B) (18). In neurons, levels of dynamin 1 increase with synapse formation in parallel with the levels of synaptic vesicle proteins (fig. S1E). These and many other observations (9, 18, 19) strongly suggest that dynamin

1 plays a dedicated and essential role in the recycling of synaptic vesicles and, thus, a critical role in nervous system function.

Dynamin 1–KO mice appear normal at birth.

A null allele of the mouse dynamin 1 gene was generated by deleting exon 1 (20) (fig. S1F). Heterozygous mice were viable, fertile, and without any apparent health defects. Their matings yielded wild-type (WT), heterozygous (Ht) and, surprisingly, knockout (KO) pups in the expected Mendelian ratio (table S1). At birth, KO mice breathed, moved, and suckled and were not distinguishable from their littermates (Fig. 1A). Thus, dynamin 1 is not required for either embryonic development or for the neurotransmission that supports perinatal life. However, a reduction in the ingestion of milk was apparent in KO pups within several hours after birth (Fig. 1A), and poor motor coordination became obvious over the following days. Overall, dynamin 1–KO pups failed to thrive and died within 2 weeks (fig. S3).

Immunoblot analysis of brain tissue and cortical neuron cultures demonstrated the absence of dynamin 1 in KO mice and a dramatic decrease of total dynamin levels (Fig. 1B and fig. S2), confirming that dynamin 1 is by far the predominant dynamin in the nervous system. Levels of dynamin 2 and 3, as well as of a variety of proteins involved in synaptic transmission and endocytosis, were not changed (Fig. 1B and fig. S2).

Synaptic transmission in dynamin 1–KO neurons. Whole-cell voltage-clamp recordings from primary cortical cultures were carried out to study the impact of the loss of dynamin 1 on synaptic transmission. Recordings of miniature excitatory and inhibitory postsynaptic currents (mEPSCs and mIPSCs, respectively) revealed a large increase (Fig. 2, A and B), possibly due to increased vesicle size (see below). Next, evoked synaptic transmission was analyzed in paired recordings from low-density cortical cultures.

¹Howard Hughes Medical Institute, Kavli Institute for Neuroscience, Yale University School of Medicine, New Haven, CT 06510, USA. ²Program in Cellular Neuroscience, Neurodegeneration and Repair, Yale University School of Medicine, New Haven, CT 06510, USA. ³Department of Cell Biology, Yale University School of Medicine, New Haven, CT 06510, USA. ⁴Section of Immunobiology, Yale University School of Medicine, New Haven, CT 06510, USA. ⁵Department of Biochemistry, Weill Medical College of Cornell University, New York, NY 10021, USA. ⁶David Rockefeller Graduate Program, The Rockefeller University, New York, NY 10021, USA. ⁷IFOM, the FIRC Institute for Molecular Oncology Foundation, and Università Vita-Salute San Raffaele, Milano, Italy. ⁸Boulder Laboratory for 3D Electron Microscopy of Cells, Department of Molecular, Cellular, and Developmental Biology, University of Colorado, Boulder, CO 80309, USA.

*These authors contributed equally.

†To whom correspondence should be addressed. E-mail: pietro.decamilli@yale.edu

Fig. 1. Dynamin 1–KO mice appear normal at birth. (A) Ht and KO pups several hours after birth. Arrows highlight less milk in the stomach of the KO pup. (B) Immunoblot analysis of cell lysates from primary cortical neuron cultures (15 to 21 DIV) with dynamin isoform-specific antibodies and a pan-dynamin antibody. Clathrin LC, clathrin light chain.

